Available online at www.sciencedirect.com
ScienceDirect
Trans. Nonferrous Met. Soc. China 35(2025) 734−748
Transactions of Nonferrous Metals Society of China
www.tnmsc.cn

A novel constitutive model for two-stage creep aging process of 7B50 aluminum alloy and its application in springback prediction

Ling-zhi XU[1,2], Can-yu TONG [1,3], Chang-zhi LIU[4], Li-hua ZHAN[2,3], Ming-hui HUANG[2,3], You-liang YANG[3], Dong-yang YAN[4], Jian-hua YIN[4], Hui XIA[4], Yong-qian XU[3]

1. AVIC General Huanan Aircraft Industry Co., Ltd., Zhuhai 519000, China;
2. State Key Laboratory of Precision Manufacturing for Extreme Service Performance, Central South University, Changsha 410083, China;
3. Light Alloy Research Institute, Central South University, Changsha 410083, China;
4. Beijing Institute of Astronautical Systems Engineering, Beijing 100076, China

Received 7 August 2023; accepted 17 April 2024

Abstract: A new unified constitutive model was developed to predict the two-stage creep-aging (TSCA) behavior of Al−Zn−Mg−Cu alloys. The particular bimodal precipitation feature was analyzed and modeled by considering the primary micro-variables evolution at different temperatures and their interaction. The dislocation density was incorporated into the model to capture the effect of creep deformation on precipitation. Quantitative transmission electron microscopy and experimental data obtained from a previous study were used to calibrate the model. Subsequently, the developed constitutive model was implemented in the finite element (FE) software ABAQUS via the user subroutines for TSCA process simulation and the springback prediction of an integral panel. A TSCA test was performed. The result shows that the maximum radius deviation between the formed plate and the simulation results is less than 0.4 mm, thus validating the effectiveness of the developed constitutive model and FE model.

Key words: two-stage creep aging process; bimodal precipitation; constitutive modeling; springback prediction; Al−Zn−Mg−Cu alloy

1 Introduction

Creep aging forming (CAF) is a reliable technology for manufacturing large panels/integral panels using high-strength aluminum alloys [1]. This technique not only enables simultaneous shaping and strengthening of components but also ensures high precision of forming and minimal residual stresses [2]. Despite its advantages, CAF encounters challenges, notably considerable springback and extended processing durations needed for shaping components, especially those made from Al−Zn−Mg−Cu alloys [1,3]. Recently, a novel two-stage creep aging (TSCA) behavior of Al−Zn−Mg−Cu alloys during a particular CAF process, which featured an elevated temperature followed by a peak-aging temperature, was investigated [4]. Improved creep-forming efficiency and bimodal precipitation features were observed during TSCA; however, a model describing TSCA is required to accurately predict its springback and facilitate potential industrial applications.

Developing unified constitutive models is crucial for CAF applications, as they provide a scientific method for predicting the ultimate shape and mechanical properties of the components manufactured. Therefore, the modeling of both the

Corresponding author: Yong-qian XU, Tel: +86-15874221120, E-mail: yongqian.xu@csu.edu.cn
DOI: https://doi.org/10.1016/S1003-6326(24)66711-7

creep deformation and aging behavior of aluminum alloys has been conducted extensively in recent decades. In 2004, HO et al [5] proposed a unified creep aging (CA) model based on the existing creep sinh law function and aging models. They introduced precipitation-related microvariables and dislocation state variables into the models, which successfully described the variation in the creep strain and yield strength of 7010 aluminum alloy at 423 K. In 2011, ZHAN et al [6] developed a mechanism-based unified CA constitutive model based on two normalized parameters, i.e., dislocation density ($\bar{\rho}$) and precipitate radius ($\bar{r}$), to simulate the interactive effect between creep and aging of a material during CAF. Their model was validated based on the experimental results of a 7055 aluminum alloy creep aged at 393 K and was subsequently used to model the CA behavior of 2219-T4 and 7050-T751 aluminum alloys. Other modified unified constitutive models, which include more specific variables, have also been reported, aiming to describe the CA behavior of different aluminum alloys or precipitate types [7,8,9].

In recent years, many advanced constitutive models have been established to describe the complex CA responses of aluminum alloys. The plastic strain occurring before creep has received significant interest, as plastic-induced dislocations typically have a considerable effect on the CA behavior [10−13]. MA et al [10] discovered that loading exceeding the yield strength not only increased the creep strain of the 2219 aluminum alloy but also enhanced the mechanical properties by promoting the heterogeneous growth of the θ' phase and eliminating the adverse stress-orienting effect. They developed a dislocation-based internal variable creep model that accounts for the interaction between loading-induced dislocations and the bimodal precipitation of θ' and θ'' phases. RONG et al [13] investigated the stress-relaxation aging (SRA) behavior of the 6082 aluminum alloy in the elastic–plastic region and established a unified SRA constitutive model, introducing a variable threshold stress under different initial stresses. The model was subsequently used to predict the springback magnitude of the 6082-T6 aluminum alloy with loaded stresses that span from elastic to plastic regions, and accurate predictions were achieved. Additionally, since compression stress typically occurs in components subjected to loading, the compression creep behavior and corresponding models have been extensively investigated [14,15]. LI et al [15,16] developed and validated a unified constitutive model to describe the asymmetric tension/compression creep behavior and double primary creep of an Al−Cu−Li alloy during CA at 428 K by considering the gradual dissolution of naturally aged precipitates and the growth of newly formed precipitates. Moreover, ZHENG et al [17,18] modeled the multistage SRA behavior of a 7050 aluminum alloy based on dynamic aging and power-law creep relations and verified the model via T74 (393 K for 6 h followed by 450 K for 7 h) multistage SRA experiments.

Although these existing models can accurately predict CA/SRA behaviors, they focus solely on isothermal processes. XU et al [19] claimed that the creep strain in the non-isothermal creep heating stage accounted for 22.28%−28.26% of the total creep strain. Therefore, the creep strain and yield strength variation during the non-isothermal stage should be adopted in the constitutive model to increase the prediction accuracy, particularly for multistage CA processes [4]. Notably, the modeling and simulation of the bimodal precipitation evolution of Al−Zn−Mg−Cu alloys during CAF have not yet been reported.

Hence, this study aims to develop a novel unified constitutive model that captures the relevant mechanisms of TSCA to accurately predict the springback of components manufactured via TSCA. This model incorporates the softening and strengthening effects of bimodal precipitation by introducing temperature-dependent terms into the microstructural equations, as well as the interrelationship of the volume fraction ($\bar{f}$) of the coarse and newly re-precipitated phases. Finite element analysis were employed to predict the springback condition of an integral panel, and the results were compared with those of a corresponding TSCA test. The developed FE model can assist in tool shape compensation and optimize the manufacturing process for creep age forming.

2 Experimental

2.1 As-received material and panel preparation

The raw material was a 7B50 aluminum alloy plate in the T651 state (1% pre-stretching plus 393 K, 24 h artificial aging) measuring 805 mm ×

600 mm × 49 mm, and the exact chemical composition is listed in Table 1. The integral panel was machined from the as-received plate, and the semi-sections of which are shown in Fig. 1.

Table 1 Chemical composition of as-received 7B50 aluminum alloy (wt.%)

Zn	Mg	Cu	Mn	Fe
6.100	2.190	2.190	0.004	0.083
Si	Ni	Cr	Ti	Al
0.048	<0.010	0.160	0.025	Bal.

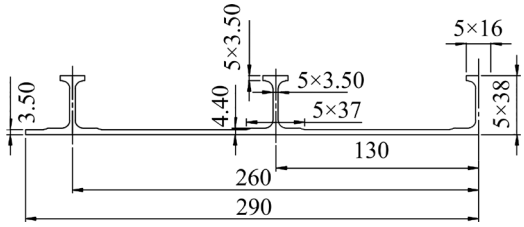

Fig. 1 Semi-section geometry and dimensions of integral panel for creep-aging forming test (unit: mm)

2.2 CAF test

A CAF test was conducted in a laboratory autoclave, where the accuracy of temperature and pressure control was ±1.5 K and ±0.01 MPa, respectively [20]. The CAF test procedure is schematically depicted in Fig. 2 and described as follows: (1) the integral panel was wrapped with a breather fabric and then placed on a single curvature mold with a radius of 480 mm (Fig. 2(a)); (2) the mold and panel were sealed using a vacuum bagging film, the air in the toolset was extracted using a vacuum pump, and the toolset was creep-aged in the autoclave under an applied pressure of 4×10^5 Pa and subjected to the aging condition shown in Fig. 3(c) (Fig. 2(b)); (3) the pressure was unloaded and the panel was allowed to springback (Fig. 2(c)).

2.3 Finite element (FE) model

Figure 3 illustrates the FE model for the TSCA process of the integral panel constructed using the ABAQUS software. A quarter-model simulation was established to reduce the computational cost of the symmetrical structure. The panel was modeled using C3D20R solid elements, and the tool surface with a radius of 480 mm was set as a rigid body. Symmetric boundary conditions were applied to the

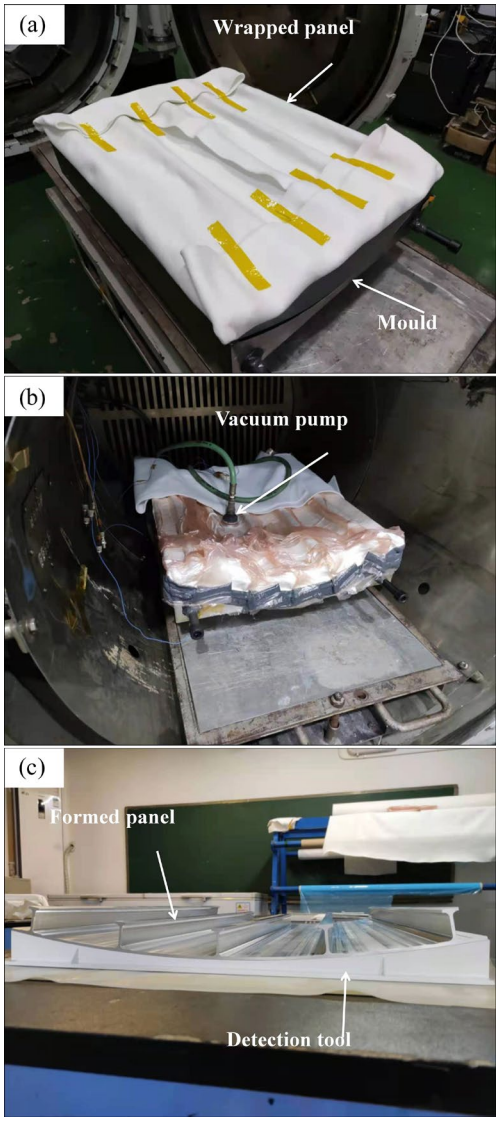

Fig. 2 Schematic illustration of creep-aging forming process: (a) Before loading; (b) Loading and being ready for creep-aging; (c) Unloading and springback

nodes along the dotted lines depicted in Fig. 3(a). The friction coefficient between the tool and panel was defined as 0.3, based on the formula for penalty friction [21]. The Young's modulus and Poisson's ratio were defined as 68 GPa and 0.3, respectively, and the room-temperature engineering stress–strain behavior of 7B50-T6 in tension state, as shown in Fig. 3(b), was imported into the model. The TSCA model included four steps: (1) The tool surface moves upward along the *Y*-axis until it makes contact with the panel; (2) A specific load, depicted in Fig. 3(c), is applied to the upper surface of the panel such that the panel is in complete contact with the tool surface; (3) The load is maintained under the temperature conditions shown in Fig. 3(c),

during which the evolution of material variables within the TSCA model is calculated via the implemented subroutine, CREEP; (4) The load is removed from the element.

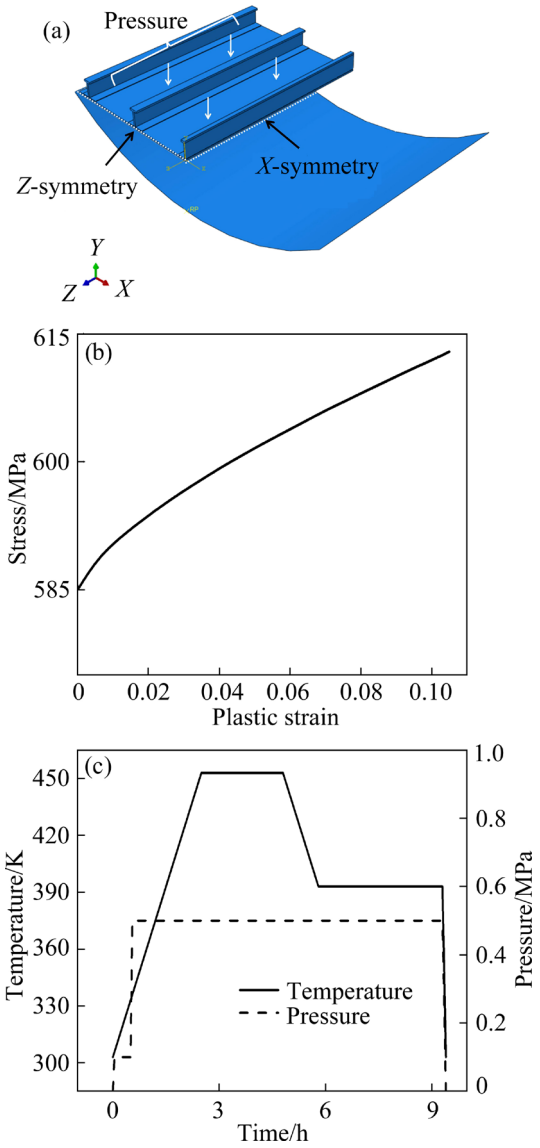

Fig. 3 FE simulation of TSCA forming process: (a) One-quarter FE model of integral panel with boundary conditions; (b) Room-temperature engineering tension stress–strain behavior of 7B50-T6 aluminum alloy; (c) Temperature and pressure loading curves during TSCA process simulation

2.4 Radius and electrical conductivity test

The radius of the creep-aged integral panel was measured using a radius detection tool with a fixed curvature, as shown in Fig. 3(c). The curvature of the detection tool was determined based on the simulation results. The creep-aged panels were subjected to electrical conductivity tests using a SIGMASCOPE SMP350 eddy-current conductivity meter in accordance with GB/T 12966—2008.

3 CA behavior and microstructural evolution of TSCA process

The CA behavior of the 7B50 aluminum alloy during TSCA has been reported in the literature [4]. Figure 4 schematically illustrates the typical creep strain curves and yield strength evolution throughout the process. This particular CA behavior can reduce the formation time while considerably improving creep-forming deformation without sacrificing strength, as compared with the conventional single-stage CA. Further details regarding the experimental setup and results are available in Ref. [4].

TEM and related differential scanning calorimetry (DSC) analyses were performed to analyze the precipitate evolution during the TSCA of the 7B50 aluminum alloy reported in Ref. [4]. A bimodal precipitate size distribution was observed, and the possible microscopic mechanisms were discussed. As shown in Fig. 4, during the heating stage, pre-aged fine Guinier-Preston (GP) zones dissolved, and the η' phase developed gradually at temperatures exceeding 423 K. This variation continued and rapidly in the subsequent soaking stage at 453 K, which deteriorated the yield strength. As the temperature decreased to 393 K, the coarsening of the large phases decelerated, and the new fine GP zones began to re-precipitate synchronously in the matrix. Subsequently, these new phases increased slightly in both size and number in the soaking stage at 393 K, thus hindering dislocation movement and resulting in a gradual increase in the mechanical strength over time. The creep strain accumulated more rapidly in the high-temperature stage compared to that observed in the conventional creep behavior because of the reduced barrier for dislocation motion and the thermally activated mechanism. Evidently, the creep deformation and precipitation processes are sensitive to the heat-treatment temperature, which should be considered in modeling.

The evolution of microstructural variables such as precipitate size and volume fraction is

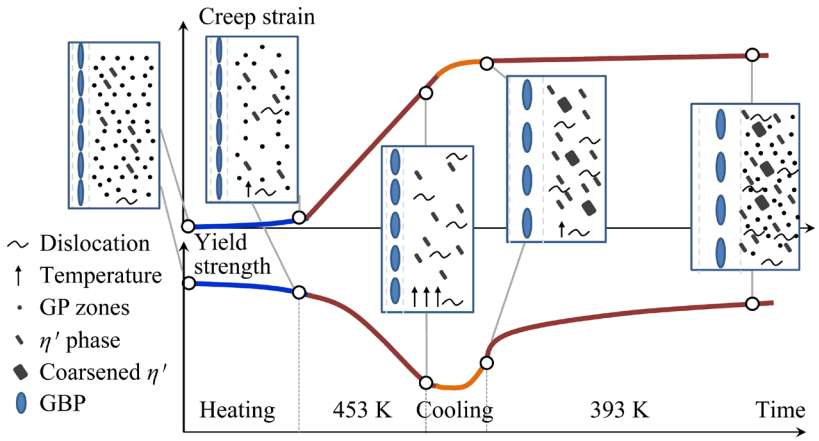

Fig. 4 Schematic illustration of evolution of microstructures of 7B50 aluminum alloy during TSCA and their relationship with creep deformation and mechanical properties [4]

crucial for developing and calibrating a unified constitutive model. Therefore, the extent of the bimodal precipitate radius (r) and number density (n) at each stage of the TSCA process were measured in an earlier study [4], as shown in Fig. 5(a). These two variables can be used to evaluate the precipitate volume fraction (f), which is expressed as [22]

$$f=4\pi r^3 n/3 \quad (1)$$

Furthermore, it can be normalized as follows:

$$\overline{f}=\frac{f}{f_e} \quad (2)$$

where f_e denotes the equilibrium volume fraction. In this study, f_e was obtained based on TEM observation as well as quantifying an over-aged sample that was heat-treated at 433 K for 16 h after peak aging and was considered to have reached its equilibrium value of precipitation. Five TEM images of different regions and at least 80 edge-on precipitates were measured; their average radius (r_e) and number density (n_e) were 10 nm and $3.5\times10^{15}/cm^3$, respectively, as shown in Fig. 5(a). Thus, the value of $\overline{f}$ at each stage can be calculated from the radii (r^3/r_e^3) and number density (n/n_e) of the phases in the creep-aged and over-aged samples. Figure 5(b) shows the evolution of $\overline{f}$ of the coarse and fine/re-precipitate phases, which indicates a considerable increase in the coarse phase and a decline in the small phase during the high-temperature stage, followed by a slight increase in both phases owing to the reduced temperature.

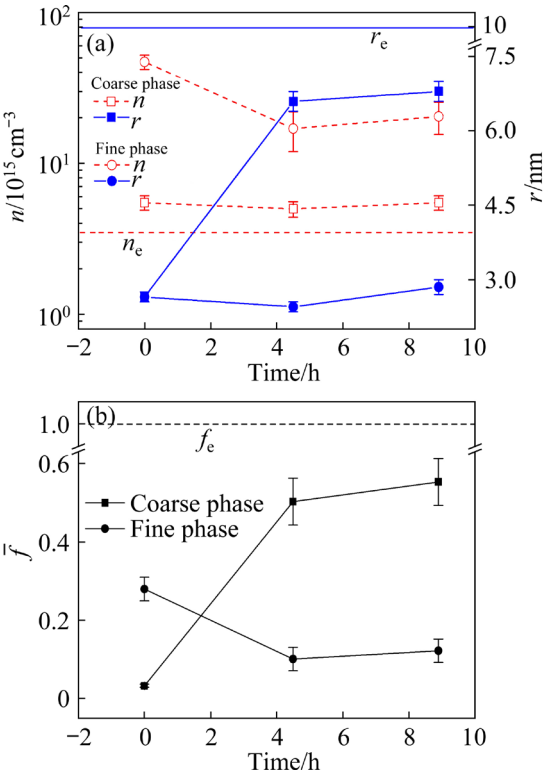

Fig. 5 Evolution of statistical average radius and number density (a), and normalized volume fraction (b) during TSCA and corresponding value of over-aged sample

4 Model development

Based on the CA behavior and bimodal precipitate evolution discussed above, this study developed a unified constitutive model to describe the variations in yield strength and creep strain of Al−Zn−Mg−Cu alloys during TSCA. The model was constructed via an internal microstructural variable approach [16,23], involving three types of

models: (1) a creep strain–stress model, (2) a strength model, and (3) microstructure models. The creep strain–stress model, based on the conventional power-law creep equation, is governed by the applied stress (σ), yield strength (σ_y), dislocation (ρ), and temperature (T), as shown in Eq. (3) [6]. The strength models allow the yield strength (σ_y) to be predicted and is defined by the precipitation (σ_{ppt}), solid solution (σ_{ss}), and dislocation strength (σ_{dis}) (Eq. (4)). All these strength components are affected by the evolution of the precipitate size (r), volume fraction (f), and dislocation density (ρ) during TSCA [24]. Similarly, the microstructural variables (V) are determined not only by the state variables and aging temperature (T) but also by the applied stress (σ) or creep strain (ε_c) (Eq. (5)).

$$\dot{\varepsilon}_c=f(\sigma,\ \sigma_y,\ \rho,\ T) \tag{3}$$

$$\sigma_y=f(\sigma_{ppt},\ \sigma_{ss},\ \sigma_{dis})=F(V) \tag{4}$$

$$\dot{V}=f\left(\sigma,\ V,\ T,\ \dot{\varepsilon}_c\right) \tag{5}$$

The modeled creep strain and yield strength are presented in Sections 4.1 and 4.2, respectively. Meanwhile, the evaluation and modeling of the evolution of the corresponding microstructural variables during TSCA are presented in Section 4.3.

4.1 Creep strain–stress model

A sinh-law creep strain–stress model that describes the relationship among the creep strain (ε_c), initial stress (σ), and yield strength (σ_y) is expressed as [6]

$$\dot{\varepsilon}_c=A\sinh\left\{B\left[\sigma\left(1-\overline{\rho}\right)-k\sigma_y\right]\right\} \tag{6}$$

where A, B, and k are material constants, and $\overline{\rho}$ is the normalized dislocation density. Moreover, as discussed in Section 3, the creep behavior of the Al−Zn−Mg−Cu alloy during TSCA is primarily governed by the aging temperature; therefore, the Arrhenius equation is introduced, and a modified creep model is established as [25,26]

$$\dot{\varepsilon}_c=A\sinh\left[\frac{B\sigma\left(1-\overline{\rho}\right)^n}{\sigma_y}\right]\exp\left(-\frac{Q}{RT}\right) \tag{7}$$

where n is a constant, Q is the creep activation energy, and R is the molar gas constant (8.314 J/K·mol).

4.2 Strength model

In the CAF process, the overall yield strength of age-hardened aluminum alloys is defined by the precipitation (σ_{ppt}), solid solution (σ_{ss}), and dislocation strengths (σ_{dis}). A classic law for all strengthening components is expressed as [27]

$$\sigma_y=\sigma_{ss}+\sqrt{\sigma_{dis}^2+\sigma_{ppt}^2} \tag{8}$$

4.2.1 Solid-solution strengthening

The solid-solution strengthening (σ_{ss}) of a material can be determined from the average concentration of the aluminum matrix ($\overline{C}$) as follows [28]:

$$\sigma_{ss}=\alpha\overline{C}^{2/3} \tag{9}$$

where α is a constant. LI et al [16] developed a relationship between the solute concentration of the matrix and the relative volume fraction ($\overline{f}$) of precipitates, as shown in Eq. (10).

$$\sigma_{ss}=C_{ss}\left(1-\overline{f}\right)^{2/3} \tag{10}$$

where C_{ss} is a constant. In this study, the relative volume fraction ($\overline{f}$) includes the relative volume fraction of coarse ($\overline{f}_c$) and fine ($\overline{f}_f$) precipitates. Thus, the solution strengthening (σ_{ss}) can be rewritten as

$$\sigma_{ss}=C_{ss}\left(1-\overline{f}_c-\overline{f}_f\right)^{2/3} \tag{11}$$

4.2.2 Dislocation strengthening

Dislocation strengthening (σ_{dis}) describes the strength enhancement arising from creep-strain-induced dislocations during CAF, which is generally expressed as [6]

$$\sigma_{dis}=C_{dis}\overline{\rho}^{n_{dis}} \tag{12}$$

where C_{dis} and n_{dis} are material constants, and n_{dis} is suggested to be approximately 0.5 [29].

4.2.3 Precipitation strengthening

During TSCA, both the coarsening of the large phase and the dissolution/re-precipitation of the fine phase contribute to the precipitation strengthening (σ_{ppt}) variation of aluminum alloys and should be modeled separately. SHERCLIFF and ASHBY [24] hypothesized that the contribution of precipitates to strength may occur via two possible mechanisms: shearing strength (σ_1) and bypassing strength (σ_2):

$$\sigma_1=C_1f^{0.5}r^{n_1} \tag{13}$$

$$\sigma_2=\frac{C_2 f^{0.5}}{r^{n_2}} \tag{14}$$

where C_1, C_2, n_1, and n_2 are constants. The shearing strength (σ_1) increases with the precipitate radius (r) and is assumed to govern the strengthening before peak aging, whereas the by-passing strength (σ_2) exhibits an opposite trend and is assumed to determine the strengthening after over-aging. Considering that the initial stage of the TSCA-treated Al−Zn−Mg−Cu alloy is the T6 peak-aging state and that the existing fine phase dominates the precipitation strengthening of the material in this initial stage [4], one can reasonably conclude that the fine phase is based on the shearing mechanism. In contrast, the coarsened phase mainly determines the precipitation strengthening during TSCA and can be assumed to be based on the bypassing mechanism.

In addition, a normalized precipitate radius ($\overline{r}$) is introduced as follows:

$$\overline{r}=\frac{r}{r_e} \tag{15}$$

where r_e is the average precipitate radius in the peak aging state, which was measured to be approximately 5 nm[4,30]. Substituting $\overline{f}$ and $\overline{r}$ into Eqs. (13) and (14) yields

$$\sigma_f=C_{\sigma_f}\overline{f}_f^{0.5}\overline{r}_f^{n_1} \tag{16}$$

$$\sigma_c=\frac{C_{\sigma_c}\overline{f}_c^{0.5}}{\overline{r}_c^{n_2}} \tag{17}$$

where C_{σ_f} and C_{σ_c} are constants, σ_f and σ_c are the strength contributions from fine and coarse precipitates, respectively; and $\overline{r}_f$ and $\overline{r}_c$ are the normalized precipitate radius of fine and coarse precipitates, respectively. The overall precipitation strengthening (σ_{ppt}) can be mathematically approximated using the harmonic mean, as described in Ref. [24].

$$\sigma_{ppt}=\left(\frac{1}{\sigma_f}+\frac{1}{\sigma_c}\right)^{-1} \tag{18}$$

4.3 Microstructure models

4.3.1 Normalized dislocation density

The normalized dislocation density ($\overline{\rho}$) is essential for describing the dislocation strengthening and creep strain model, which was first defined in Ref. [6] as follows:

$$\overline{\rho}=\frac{\rho-\rho_i}{\rho_m} \tag{19}$$

where ρ_i is the dislocation density of the initial material, and ρ_m is the saturated dislocation density. Here, $\overline{\rho}$ varies from 0 to 1 and evolves based on Eq. (20) [18].

$$\dot{\overline{\rho}}=C_{\rho_1}\left(1-\overline{\rho}\right)\dot{\varepsilon}_c-C_{\rho_2}\exp\left(-\frac{Q_\rho}{RT}\right)\overline{\rho}^{n_\rho} \tag{20}$$

where C_{ρ_1} is the material constant that describes dislocation accumulation due to creep strain, whereas C_{ρ_2} and n_ρ are constants that characterize dislocation annihilation by dynamic recovery. The dislocation recovery effect is enhanced as the temperature increases; hence, the Arrhenius equation is introduced, where Q_ρ is the activation energy.

4.3.2 Normalized precipitate radius

The precipitation behavior of aluminum alloys during CA has been extensively investigated recently. The variation in precipitate size depends not only on the aging temperature and time, but also on the dislocation introduced by the creep strain. This variation can be expressed as [6]

$$\dot{\overline{r}}=C_r\left(\overline{R_s}-\overline{r}\right)^{n_3}\left(1+k_r\overline{\rho}^{n_4}\right) \tag{21}$$

where C_r, k_r, n_3, and n_4 are material constants; and $\overline{R_s}$ represents the saturation state of the precipitate growth, which depends on the aging temperature. Thus, when $\overline{r}=\overline{R_s}$, the growth rate of the precipitate radius reaches zero at a constant temperature. The $\overline{R_s}-T$ relationship between fine and coarse precipitates was established separately based on the DSC results [4,31] as follows:

$$\overline{R_{sf}}=\overline{R_{sf0}}-\exp[k_f(T-453)] \tag{22}$$

$$\overline{R_{sc}}=\overline{R_{sc0}}\exp[k_c(T-303)] \tag{23}$$

where k_f and k_c are constants, and $\overline{R_{sf0}}$ and $\overline{R_{sc0}}$ are the initial saturation radii of the fine and coarse precipitates, respectively, at the beginning of TSCA, and should be 1 because of the initial T6 peak-aging state. Equation (22) describes the complete dissolution of fine precipitates when the temperature approaches 453 K, and the re-precipitation when the temperature decreases. Equation (23) expresses the monotonic growth of the coarse precipitates with increasing temperature.

Substituting Eqs. (22) and (23) into Eq. (21) yields

$$\dot{\bar{r}}_{\mathrm{f}}=C_{\mathrm{rf}}\left(1-\exp[k_{\mathrm{f}}(T-453)]-\bar{r}_{\mathrm{f}}\right)^{n_{3\mathrm{f}}}\left(1+k_{\mathrm{rf}}\bar{\rho}^{n_{4\mathrm{f}}}\right) \tag{24}$$

$$\dot{\bar{r}}_{\mathrm{c}}=C_{\mathrm{rc}}\left(\exp[k_{\mathrm{c}}(T-303)]-\bar{r}_{\mathrm{c}}\right)^{n_{3\mathrm{c}}}\left(1+k_{\mathrm{rc}}\bar{\rho}^{n_{4\mathrm{c}}}\right) \tag{25}$$

where C_{rf}, C_{rc}, $n_{3\mathrm{f}}$, $n_{3\mathrm{c}}$, k_{rf}, k_{rc}, $n_{4\mathrm{f}}$, and $n_{4\mathrm{c}}$ are material constants.

4.3.3 Normalized volume fraction

The volume fraction of precipitates during aging is typically assumed to be related to both the aging time and the particle size [32]. Moreover, in CAF, the dislocations caused by creep strain promote precipitation by providing heterogeneous nucleation sites and serving as rapid diffusion paths[10]. Given that the effects of dislocations and temperature on precipitation are considered in Eqs. (24) and (25), the evolution of the normalized volume fraction of fine and coarse precipitates can thus be expressed as [25]

$$\dot{\bar{f}}_{\mathrm{f}}=C_{\mathrm{ff}}\frac{\bar{r}_{\mathrm{f}}^{3}}{q_{\mathrm{f}}}\dot{\bar{r}}_{\mathrm{f}}\left(1-\bar{f}_{\mathrm{c}}-\bar{f}_{\mathrm{f}}\right) \tag{26}$$

$$\dot{\bar{f}}_{\mathrm{c}}=C_{\mathrm{fc}}\frac{\bar{r}_{\mathrm{c}}^{3}}{q_{\mathrm{c}}}\dot{\bar{r}}_{\mathrm{c}}\left(1-\bar{f}_{\mathrm{f}}\right) \tag{27}$$

where C_{ff} and C_{fc} are material constants, and $q=r/l$ is the aspect ratio, where l is the thickness of the precipitate. Thus, q_{f} and q_{c} are calculated to be 1.25 and 1.3, respectively, based on the data in Ref. [4].

4.4 Model implementation and validation

4.4.1 Determination of material constants

Based on the analyses above, a set of unified constitutive models that describe the creep-aging behavior of Al−Zn−Mg−Cu alloys during TSCA process is derived as follows:

$$\dot{\varepsilon}_{\mathrm{c}}=A\sinh\left[\frac{B\sigma\left(1-\bar{\rho}\right)^{n}}{\sigma_{\mathrm{y}}}\right]\exp\left(-\frac{Q}{RT}\right) \tag{28}$$

$$\sigma_{\mathrm{y}}=\sigma_{\mathrm{ss}}+\sqrt{\sigma_{\mathrm{dis}}^{2}+\sigma_{\mathrm{ppt}}^{2}} \tag{29}$$

$$\sigma_{\mathrm{ss}}=C_{\mathrm{ss}}\left(1-\bar{f}_{\mathrm{c}}-\bar{f}_{\mathrm{f}}\right)^{2/3} \tag{30}$$

$$\sigma_{\mathrm{dis}}=C_{\mathrm{dis}}\bar{\rho}^{n_{\mathrm{dis}}} \tag{31}$$

$$\sigma_{\mathrm{ppt}}=\left(\frac{1}{\sigma_{\mathrm{f}}}+\frac{1}{\sigma_{\mathrm{c}}}\right)^{-1} \tag{32}$$

$$\sigma_{\mathrm{f}}=C_{\sigma_{\mathrm{f}}}\bar{f}_{\mathrm{f}}^{0.5}\bar{r}_{\mathrm{f}}^{n_{1}} \tag{33}$$

$$\sigma_{\mathrm{c}}=C_{\sigma_{\mathrm{c}}}\bar{f}_{\mathrm{c}}^{0.5}/\bar{r}_{\mathrm{c}}^{n_{2}} \tag{34}$$

$$\dot{\bar{r}}_{\mathrm{f}}=C_{\mathrm{rf}}\left(1-\exp[k_{\mathrm{f}}(T-453)]-\bar{r}_{\mathrm{f}}\right)^{n_{3\mathrm{f}}}\left(1+k_{\mathrm{rf}}\bar{\rho}^{n_{4\mathrm{f}}}\right) \tag{35}$$

$$\dot{\bar{r}}_{\mathrm{c}}=C_{\mathrm{rc}}\left(\exp[k_{\mathrm{c}}(T-303)]-\bar{r}_{\mathrm{c}}\right)^{n_{3\mathrm{c}}}\left(1+k_{\mathrm{rc}}\bar{\rho}^{n_{4\mathrm{c}}}\right) \tag{36}$$

$$\dot{\bar{f}}_{\mathrm{f}}=C_{\mathrm{ff}}\frac{\bar{r}_{\mathrm{f}}^{3}}{1.25}\dot{\bar{r}}_{\mathrm{f}}\left(1-\bar{f}_{\mathrm{c}}-\bar{f}_{\mathrm{f}}\right) \tag{37}$$

$$\dot{\bar{f}}_{\mathrm{c}}=C_{\mathrm{fc}}\frac{\bar{r}_{\mathrm{c}}^{3}}{1.3}\dot{\bar{r}}_{\mathrm{c}}\left(1-\bar{f}_{\mathrm{f}}\right) \tag{38}$$

$$\dot{\bar{\rho}}=C_{\rho_{1}}\left(1-\bar{\rho}\right)\dot{\varepsilon}_{\mathrm{c}}-C_{\rho_{2}}\exp\left(-\frac{Q_{\rho}}{RT}\right)\bar{\rho}^{n_{\rho}} \tag{39}$$

where A, B, Q, Q_{ρ}, C_{ss}, C_{dis}, $C_{\sigma\mathrm{f}}$, $C_{\sigma\mathrm{c}}$, C_{rf}, C_{rc}, C_{ff}, C_{fc}, $C_{\rho1}$, $C_{\rho2}$, k_{f}, k_{c}, k_{rf}, k_{rc}, n, n_1, n_2, $n_{3\mathrm{f}}$, $n_{3\mathrm{c}}$, $n_{4\mathrm{f}}$, $n_{4\mathrm{c}}$, n_{dis}, and n_{ρ} are material constants. The initial values (T6 peak aging state and time 0) for the equations are listed in Table 2. The initial yield strength, normalized precipitate radius, and volume fraction were obtained from Section 3 and the literature [4].

Table 2 Estimated initial values of variables for 7B50 aluminum alloy subjected to TSCA

$\varepsilon_{\mathrm{c}0}$	$\sigma_{\mathrm{y}0}$/MPa	$\overline{r_{\mathrm{f}0}}$	$\overline{r_{\mathrm{c}0}}$	$\overline{f_{\mathrm{f}0}}$	$\overline{f_{\mathrm{c}0}}$	$\overline{\rho_0}$
0	585	1	1	0.28	0.05	1×10^{-5}

The particle swarm optimization algorithm and manual multistep fitting processes are typically adopted to determine the material constant values of the CA constitutive model [10,25]. In this study, creep strain curves with different applied stresses and soaking time at 453 K were initially fitted separately with polynomials to acquire the creep strain rate in a functional form instead of scattering points. The material constants related to the microstructure and strength models were determined by substituting polynomials into the dislocation evolution equation. Finally, the obtained parameters were used to unify Eq. (7), and all the constants were obtained, as listed in Table 3.

4.4.2 Model validation and discussion

The predicted evolutions of the macro- and micro-variables were compared with the experimental results, as shown in Fig. 6. The predicted evolution curves agreed well with the experimental data, thus confirming the effectiveness

Table 3 Material constants for TSCA of 7B50 aluminum alloy

A	B	Q/(kJ·mol^{-1})	Q_ρ/(kJ·mol^{-1})	C_{ss}	C_{dis}	$C_{\sigma f}$
1.8185×10^{6}	6.8225	9×10^{4}	4×10^{4}	180	120	2830
$C_{\sigma c}$	C_{rf}	C_{rc}	C_{ff}	C_{fc}	$C_{\sigma 1}$	$C_{\sigma 2}$
2830	0.10186	1.5736×10^{-4}	2.4526	1×10^{-4}	100	0.6
k_f	k_c	k_{rf}	k_{rc}	n	n_1	n_2
0.56888	4.5244×10^{-2}	1	1	1×10^{-5}	8×10^{-5}	1
n_{3f}	n_{3c}	n_{4f}	n_{4c}	n_{dis}	n_ρ	
1	1	1	1	0.5	4	

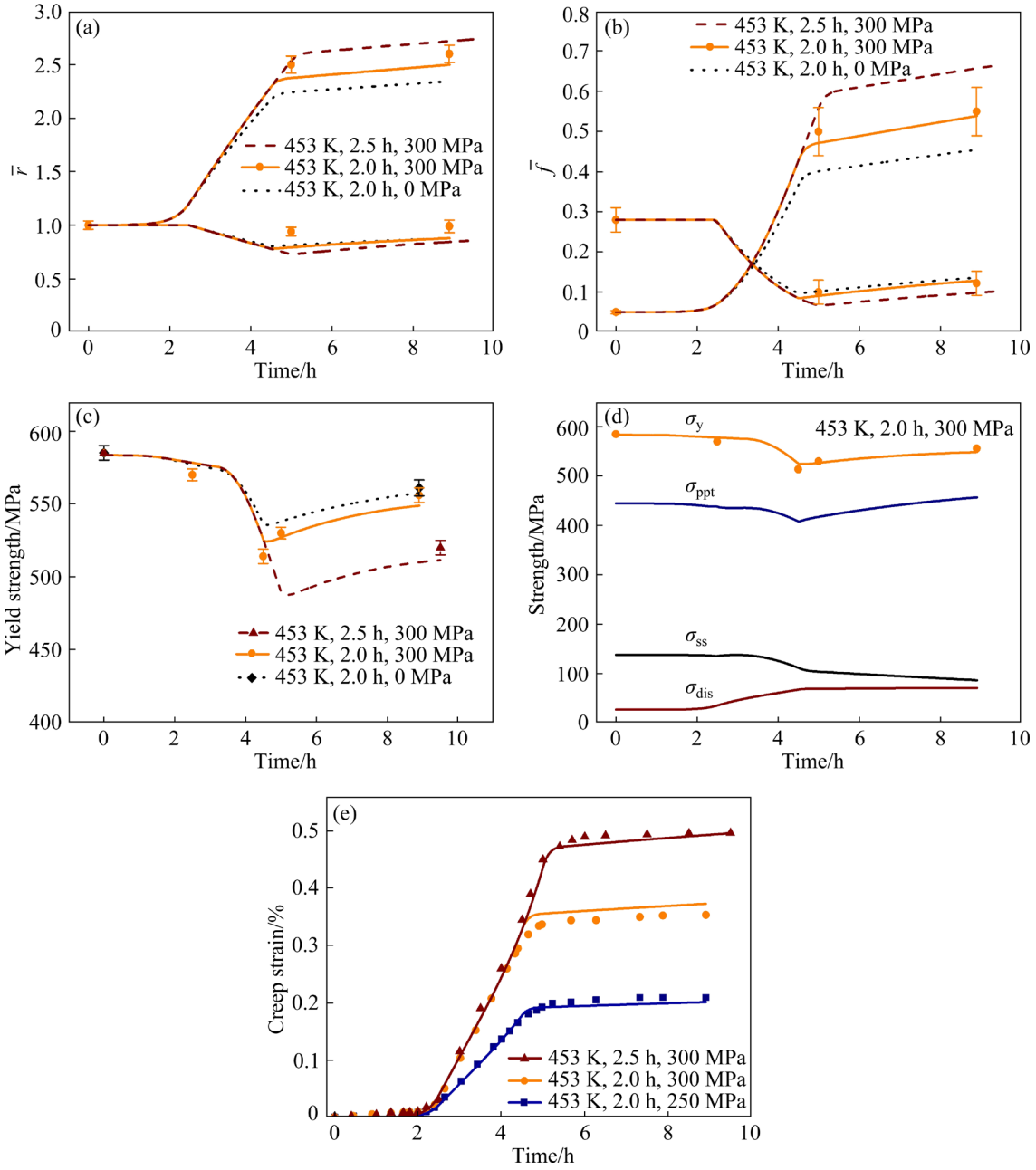

Fig. 6 Comparison of predicted (lines) and experimental (symbols) TSCA behaviors: (a) Normalized radius of bimodal precipitates; (b) Normalized volume fraction of bimodal precipitates; (c) Yield strength; (d) Different strengthening components; (e) Creep strain

of the established constitutive model and the material constants proposed herein. Moreover, the predicted microstructure and yield strength evolution during the TSCA under a holding time of 2.5 h at 453 K and pure aging (including cases without experimental data) are plotted in Fig. 6 to demonstrate the adaptability of the established constitutive model.

As shown in Figs. 6(a) and (b), the normalized precipitate radius and volume fraction evolved briefly at the beginning of the heating stage because of the low temperature. Some precipitates began to grow and coarsen above 423 K, while others dissolved at 453 K. As the growth and dissolution continued in the subsequent soaking stage at 453 K, the increasing discrepancy in the microstructural variables between the coarse and fine precipitates led to a bimodal precipitate in the matrix. These discrepancies became more evident as the soaking time increased at 453 K because further coarsening of the precipitates consumed more solute atoms, thus reducing the solute available for re-precipitation. Similarly, the applied stress can amplify the discrepancy as it promotes the coarsening of the precipitates.

Figure 6(c) presents the predicted overall yield strength evolution and experimental results for the 7B50 aluminum alloy under a 300 MPa load and 2 h of holding time at 453 K. The contributions of the different strengthening mechanisms calculated using the model are plotted as well. Dislocation strengthening increased with the dislocation density induced by creep strain, whereas solid-solution strengthening declined gradually as solute atoms in the matrix were consumed. Meanwhile, precipitation strengthening declined before the cooling stages owing to precipitation coarsening and dissolution, followed by an increase during the cooling and re-aging stages owing to the re-precipitation of the fine phase. The yield strength varied in the same manner as the precipitation strengthening and approached the initial value at the end of the TSCA. Similar to the observation of other 7xxx aluminum alloys, stress levels affect the yield strength during CAF [17,33,34]. As shown in Fig. 6(d), the yield strength under an applied stress of 0 MPa was slightly higher than that under 300 MPa, beginning from the 453 K soaking stage. This is because the dislocations introduced by creep strain promote precipitation, thus presenting the effect of stress on precipitation strengthening, as confirmed by Eqs. (24) and (25). Similarly, extending the soaking time at 453 K facilitated the coarsening of precipitates and significantly reduced the yield strength.

The experimental results and modeled creep strains under different stresses with 2 h of soaking time at 453 K and under 300 MPa with 2.5 h of soaking time at 453 K are illustrated in Fig. 6(e). All the predicted curves agreed well with the experimental results, and the two-stage creep features were predicted accurately. This comparison confirms that the established constitutive model and material constants can accurately predict the TSCA process at 453 K with different soaking time.

5 Simulation results and experiment validation

5.1 FE simulation results

To further validate the effectiveness of the developed constitutive model, an FE model of the TSCA process for an integral panel was established using the ABAQUS software. The constitutive model was programmed in FORTRAN and implemented in ABAQUS using the user-defined subroutine CREEP. A detailed definition of the FE model is provided in Section 2.2. Figure 7 shows the von Mises stress distribution in the panel after loading. Clearly, the stress level in the stiffeners was significantly lower than that on the skin, as the curvature direction of the axial stiffeners was perpendicular to the mold. The stress level of the skin surface exceeded that of the central layer, and a maximum value of approximately 350 MPa was indicated at the root of the stiffeners. Furthermore, the stress distribution below the yield stress (Fig. 2(b)) indicated that no initial plastic strain occurred after loading.

After 9 h of the CA simulation, which included the heating stage, a creep strain developed in the integral panel, causing it to return to a certain shape. As shown in Fig. 8(a), the equivalent creep strain was mainly generated on the upper and lower surfaces of the skin, which contributed to the final shape of the panel. For a quantitative analysis, the variations in the equivalent von Mises stress and creep strain of two selected nodes on the skin surface are plotted in Figs. 8(b) and (c), respectively. As shown in Fig. 8(b), the stress of Node 1 decreased

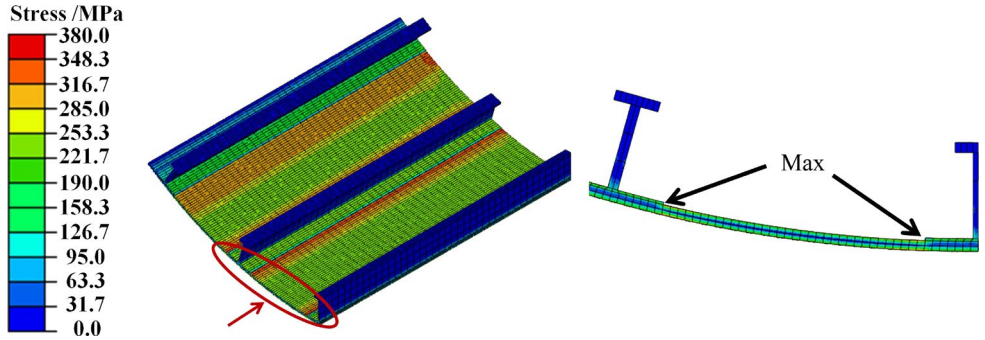

Fig. 7 Equivalent von Mises stress distribution of panel after loading

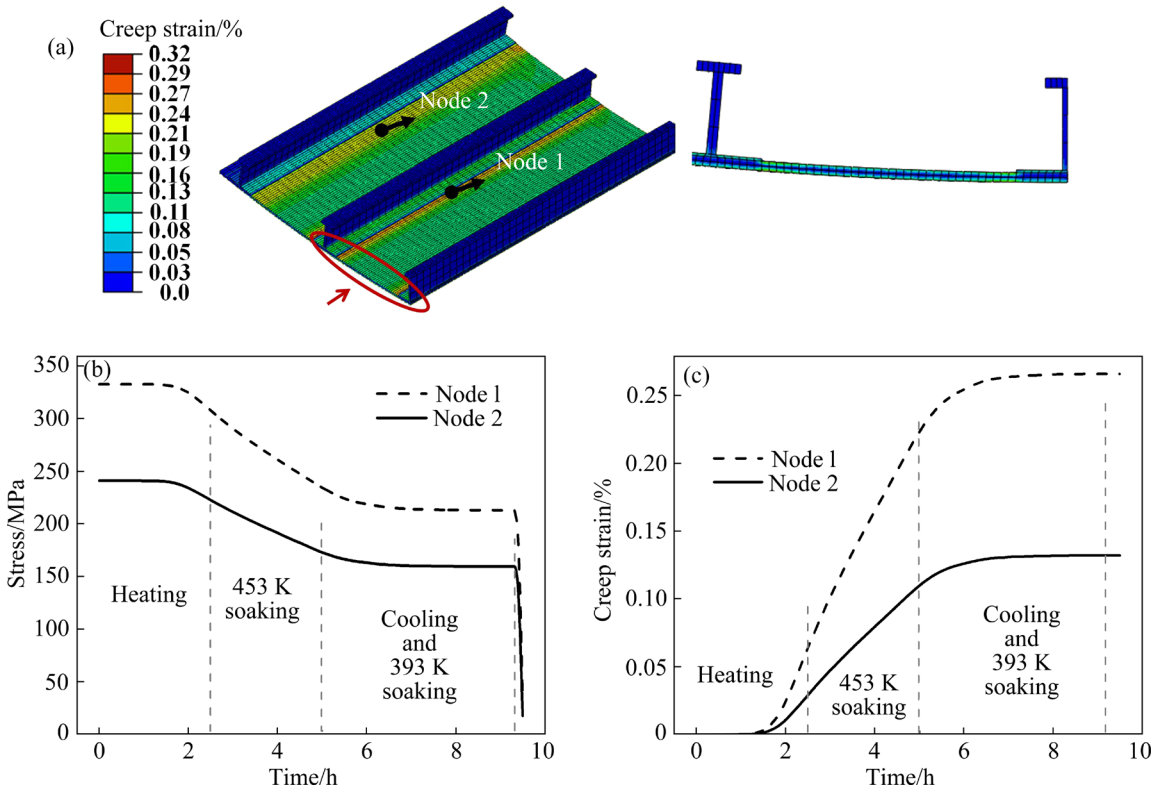

Fig. 8 Final equivalent creep strain distribution of panel (a), equivalent von Mises stress (b), and equivalent creep strain evolution (c) of selected node during TSCA simulation

from 332 to 212 MPa, and the stress of Node 2 decreased from 240 to 159 MPa, thereby indicating that a higher initial stress level results in a greater reduction in stress. Similarly, the final creep strain of Node 1 is greater than that of Node 2, as shown in Fig. 8(c). In addition, considerable creep deformation occurred during the heating stage of CAF. Based on Fig. 8(c), the creep strain during the heating stage constituted approximately 23% of the total creep strain. Therefore, the consideration of the heating stage in the CAF simulation is conducive to improving the springback prediction accuracy. Figure 9 shows the final yield strength distribution of the panel. In contrast to the stress and strain distribution, the strength of stiffener was approximately 20 MPa higher than that of the skin surface. This is because a high initial stress level adversely affects the yield strength, as shown in Fig. 6(c).

5.2 Experiment validation and discussion

The TSCA test was performed under the same process parameters as the FE model. The setup of the TSCA test is described in Section 2.3. The springback of a creep-formed panel is typically calculated as SP=$(1-R_0/R_f)\times100\%$, where R_0 and R_f are the outer surface radii of the panel before and after unloading, respectively [35]. In this study, R_0

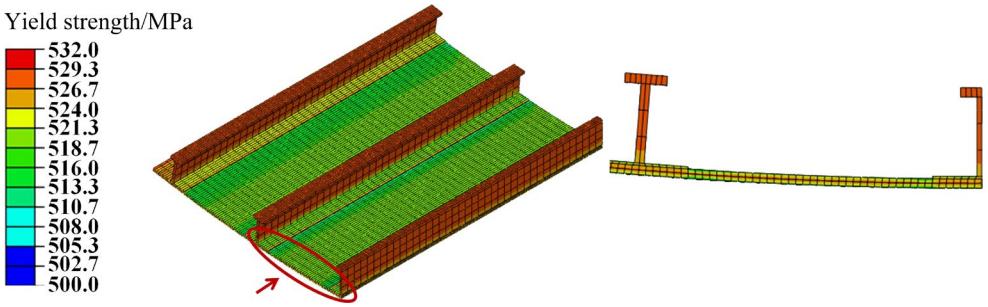

Fig. 9 Final yield strength distribution of formed panel

was 480 mm and the simulated R_f was measured in ABAQUS to be (1438±8) mm; therefore, the average springback of the simulated panel was 66.6%. Subsequently, a radius detection tool with a fixed curvature of 1400 mm was used to determine the deviation between the experimental and simulated panels. As shown in Fig. 10, the detection tool shows consistency with the outer surface of the formed panel, with the maximum deviation being less than 0.4 mm at the outboard stiffener. This may be caused by the different bending moments at the middle, left, and right sides of the panel during the loading process, which generated a small gap between the panel and mold, thus resulting in insufficient deformation on the left/right sides of the panel [20,35]. The following two factors may have contributed to the consistency mentioned above: (1) Creep deformation was considered in the heating stage; (2) Neither complex ring and side stiffeners nor double-curved shapes of the integral panel were included in this study, thereby disregarding the effect of anisotropic CA behavior on springback. Therefore, a further validation of the proposed constitutive model using panels with more complex structures is required.

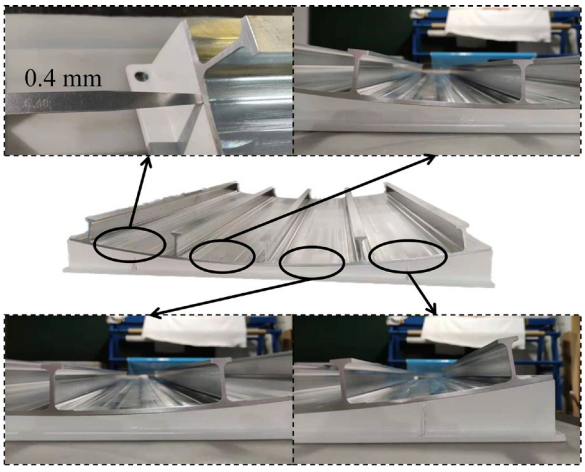

Fig. 10 Comparison of outer surface of formed plate and detection tool with fixed curvature of 1400 mm

The electrical conductivity of the formed panel was measured, and the results are shown in Fig. 11. In general, the average electrical conductivity at different positions on the panel varied from 39.4 to 39.9% (IACS), consistent with the experimental results from previous investigations; in particular, a value above 39% (IACS) was indicated when the holding time exceeded 2.5 h at 453 K [4]. According to previous investigations, the yield was approximately 520 MPa for creep-aged samples under the same TSCA conditions, thus confirming the validity of the FE and constitutive models for predicting the yield strength in CAF.

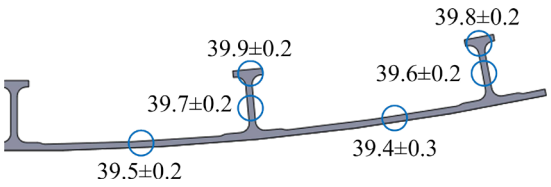

Fig. 11 Electrical conductivity of TSCA-formed panel (% (IACS))

The good agreement between the experimental and simulated results demonstrates the accuracy of the developed material model; thus, it can be used to assist tool shape compensation for the TSCA manufacturing of products made from 7B50 aluminum alloy. In addition, the model exhibits significant potential for optimizing the manufacturing process, e.g., to achieve better properties for the investigated integral panel through reduced processing time at 453 K and a smaller mold radius to satisfy the requirements of various industrial applications.

6 Conclusions

(1) A new unified constitutive model was developed to describe the newly observed CA behavior of 7B50 aluminum alloy during TSCA and compared with experimental results. The model effectively captured the bimodal precipitation mechanisms and accurately described the two-stage non-isothermal creep behavior during TSCA. It was validated for TSCA processes involving a range of applied stresses, temperatures, and holding time at 453 K, thus allowing the application of the relevant equations for optimizing manufacturing processes pertaining to TSCA.

(2) An FE model that integrates a unified constitutive model to simulate the TSCA process of an integral panel with a single-curvature bending radius of 480 mm was established for the first time. The final shape and springback of the simulated panel were measured to be (1438±8) mm and 66.6%, respectively, which were contributed by the creep strain on the skin. The final yield strength of the stiffener was 20 MPa higher than that of the skin.

(3) The springback prediction accuracy of the numerical TSCA process was validated via a corresponding forming test. The outer surface curvature of the TSCA integral panel was measured using a tool with a 1400 mm single curvature bending radius, and the measured maximum deviation was less than 0.4 mm, thus verifying the effectiveness of the developed FE model for simulating actual TSCA applications.

(4) The good agreement between the conductivities of the experimentally formed panel and the test specimens from previous investigations confirmed that the developed FE model is capable of predicting yield strength. However, for broader industrial application, the FE model should be applied to more complex integral panels, or the strengths of the formed components should be measured directly.

CRediT authorship contribution statement

Ling-zhi XU: Methodology, Formal analysis, Writing − Original draft, Writing − Review & editing; **Can-yu TONG:** Methodology, Formal analysis, Writing − Original draft, Writing − Review & editing, Visualization; **Chang-zhi LIU:** Supervision, Investigation; **Li-hua ZHAN:** Conceptualization, Methodology, Validation, Investigation, Resources, Writing − Review & editing, Supervision, Project administration, Funding acquisition; **Ming-hui HUANG:** Investigation, Resources, Supervision, Project administration, Funding acquisition; **You-liang YANG:** Writing − Review & editing, Supervision, Project administration; **Dong-yang YAN**, **Jian-hua YIN** and **Hui XIA:** Supervision, Investigation; **Yong-qian XU:** Conceptualization, Methodology, Formal analysis, Writing − Review & editing.

Declaration of competing interest

The authors declare that they have no known competing financial interests or personal relationships that could have appeared to influence the work reported in this paper.

Acknowledgments

This work was supported by the National Key R&D Program of China (No. 2021YFB3400900), the National Natural Science Foundation of China (Nos. 52175373, 52205435), Natural Science Foundation of Hunan Province, China (No. 2022JJ40621), and the Innovation Fund of National Commercial Aircraft Manufacturing Engineering Technology Center, China (No. COMAC-SFGS-2022-1875).

References

[1] ZHANG Li-wen, LI Heng, BIAN Tian-jun, WU Chang-hui, GAO Yang, LEI Chao. Advances and challenges on springback control for creep age forming of aluminum alloy [J]. Chinese Journal of Aeronautics, 2022, 35(10): 8−34.

[2] ZHAN Li-hua, LIN Jian-guo, DEAN T A. A review of the development of creep age forming: Experimentation, modelling and applications [J]. International Journal of Machine Tools and Manufacture, 2011, 51(1): 1−17.

[3] WANG Qing, ZHAN Li-hua, XU Yong-qian, LIU Chun-hui, ZHAO Xing, XU Ling-zhi, YANG You-liang, CAI Yi-xian. Creep aging behavior of retrogression and re-aged 7150 aluminum alloy [J]. Transactions of Nonferrous Metals Society of China, 2020, 30(10): 2599−2612.

[4] XU Ling-zhi, TONG Can-yu, ZHAN Li-hua, XU Yong-qian, LIU Chun-hui, HUANG Ming-hui, YANG You-liang. MA Bo-lin, WANG Yong-mei. Improved creep forming efficiency and retained performance via a novel two-stage creep aging process of Al−Zn−Mg−Cu alloys [J]. Materials Science and Engineering: A, 2022, 851: 143581.

[5] HO K C, LIN Jian-guo, DEAN T A. Constitutive modelling of primary creep for age forming an aluminium alloy [J]. Journal of Materials Processing Technology, 2004, 153/154: 122−127.

[6] ZHAN Li-hua, LIN Jian-guo, DEAN T A, HUANG Ming-hui. Experimental studies and constitutive modelling of the hardening of aluminium alloy 7055 under creep age forming

conditions [J]. International Journal of Mechanical Sciences, 2011, 53(8): 595−605.

[7] LI He, ZHAN Li-hua, HUANG Ming-hui, ZHAO Xing, ZHOU Chang, HU Li-bin, HU Zheng-gen, LIU De-bo. A unified constitutive model for multiphase precipitation and multi-stage creep ageing behavior of Al−Cu−Li alloy [J]. Transactions of Nonferrous Metals Society of China, 2021, 31(5): 1217−1234.

[8] YANG Yo-lun, LAM AARON C L, SHI Zhu-sheng, LIN Jian-guo, SAID R. Constitutive modelling of creep-ageing behaviour of peak-aged aluminium alloy 7050 [J]. MATEC Web of Conferences, 2015, 21: 12008.

[9] LI Chao, WAN Min, WU Xiang-dong, HUANG Lin. Constitutive equations in creep of 7B04 aluminum alloys [J]. Materials Science and Engineering: A, 2010, 527: 3623−3629.

[10] MA Zi-yao, ZHAN Li-hua, LIU Chun-hui, XU Ling-zhi, XU Yong-qian, MA Pei-pei, LI Jian-jun. Stress-level-dependency and bimodal precipitation behaviors during creep ageing of Al−Cu alloy: Experiments and modeling [J]. International Journal of Plasticity, 2018, 110: 183−201.

[11] XU Yong-qian, ZHAN Li-hua, LI Wen-ke. Effect of pre-strain on creep aging behavior of 2524 aluminum alloy [J]. Journal of Alloys and Compounds, 2017, 691: 564−571.

[12] YANG You-liang, ZHAN Li-hua, LIU Chun-hui, WANG Xun, WANG Qing, TANG Zhi-mao, LI Guo-peng, HUANG Ming-hui, HU Zheng-gen. Stress-relaxation ageing behavior and microstructural evolution under varying initial stresses in an Al−Cu alloy: Experiments and modeling [J]. International Journal of Plasticity, 2020, 127: 102646.

[13] RONG Qi, SHI Zhu-sheng, LI Yong, LIN Jian-guo. Constitutive modelling and its application to stress-relaxation age forming of AA6082 with elastic and plastic loadings [J]. Journal of Materials Processing Technology, 2021, 295: 117168.

[14] CHEN Kai-liang, LIU Chun-hui, MA Pei-pei, YANG Jian-shi, ZHAN Li-hua, HUANG Ming-hui, HU Jian-hua. Enhancing creep formability and comprehensive property in Al−Mg−Si alloy by combinatorial pre-ageing and large pre-deformation [J]. Materials Science and Engineering: A, 2021 826(7): 141967.

[15] LI Yong, SHI Zhu-sheng, LIN Jian-guo, YANG Yo-lun, HUANG Bo-Ming, CHUNG Tsai-fu, YANG Jer-ren. Experimental investigation of tension and compression creep-ageing behaviour of AA2050 with different initial states [J]. Materials Science and Engineering: A, 2016, 657: 299−308.

[16] LI Yong, SHI Zhu-sheng, LIN Jian-guo, YANG Yo-lun, RONG Qi, HUANG Bo-Ming, CHUNG T F, TSAO C S, YANG J R, BALINT D S. A unified constitutive model for asymmetric tension and compression creep-ageing behaviour of naturally aged Al−Cu−Li alloy [J]. International Journal of Plasticity, 2017, 89: 130−149.

[17] ZHENG Jing-hua, PAN Ran, LI Chen, ZHANG Wei, LIN Jiang-guo, DAVIES C M. Experimental investigation of multi-step stress-relaxation-ageing of 7050 aluminium alloy for different pre-strained conditions [J]. Materials Science and Engineering: A, 2018, 710: 111−120.

[18] ZHENG Jing-hua, LIN Jian-guo, LEE Jun-yi, PAN Ran, LI Chen, DAVIES C M. A novel constitutive model for multi-step stress relaxation ageing of a pre-strained 7xxx series alloy [J]. International Journal of Plasticity, 2018, 106: 31−47.

[19] XU Yong-qian, ZHAN Li-hua, HUANG Ming-hui, SHEN Ru-lin, MA Zi-yao, XU Ling-zhi, WANG Kai, WANG Xun. Deformation behavior of Al−Cu−Mg alloy during non-isothermal creep age forming process [J]. Journal of Materials Processing Technology, 2018, 255: 26−34.

[20] YANG You-liang, ZHAN Li-hua, MA Qiang-qiang, FENG Jing-wen, LI Xian-meng. Effect of pre-deformation on creep age forming of AA2219 plate: Springback, microstructures and mechanical properties [J]. Journal of Materials Processing Technology, 2016, 229: 697−702.

[21] WANG Kai, ZHAN Li-hua, YANG You-liang, MA Zi-yao, LI Xi-cai, LIU Jian. Constitutive modeling and springback prediction of stress relaxation age forming of pre-deformed 2219 aluminum alloy [J]. Transactions of Nonferrous Metals Society of China, 2019, 29(6): 1152−1160.

[22] AKHLAGHI M, STEINER T, MEKA S R, LEINEWEBER A, MITTEMEIJER E J. Lattice-parameter change induced by accommodation of precipitate/matrix misfit; misfitting nitrides in ferrite [J]. Acta Materialia, 2015, 98: 254−262.

[23] ESMAEILI S, LLOYD D J, POOLE W J. A yield strength model for the Al−Mg−Si−Cu alloy AA6111 [J]. Acta Materialia, 2003, 51 (8): 2243−2257.

[24] SHERCLIFF H R, ASHBY M F. A process model for age hardening of aluminium alloys: I. The model [J]. Acta Metallurgica et Materialia, 1990, 38: 1789−1802.

[25] YANG You-liang, ZHAN Li-hua, SHEN Ru-lin, YIN Xu-ni, LI Xian-meng, LI Wen-ke, HUANG Ming-hui, HE Di-qiu. Effect of pre-deformation on creep age forming of 2219 aluminum alloy: Experimental and constitutive modeling [J]. Materials Science and Engineering: A, 2017, 683: 227−235.

[26] XU Fu-shun, TAN Jia, ZHANG Jin, DENG Yun-lai. Modeling of the temperature-related two-stage creep aging for Al−Zn−Mg−Cu aluminum alloy [J]. Rare Metal Materials and Engineering, 2018, 47(2): 496−502.

[27] KOCKS U F, ARGON A S, ASHBY M F. Models for macroscopic slip [J]. Progress in Materials Science, 1975, 19: 171−229.

[28] WANG Shun-cai, STARINK M J. Precipitates and intermetallic phases in precipitation hardening Al−Cu−Mg−(Li) based alloys [J]. International Materials Reviews, 2005, 50(4): 193−215.

[29] TAYLOR G I. The mechanism of plastic deformation of crystals. Part I. Theoretical [J]. Proceedings of the Royal Society of London A, 1934, 145: 362−387.

[30] LIU J Z, CHEN J H, YANG X B, REN S, WU C L, XU H Y, ZOU J. Revisiting the precipitation sequence in Al−Zn−Mg−based alloys by high-resolution transmission electron microscopy [J]. Scripta Materialia, 2010, 63(11): 1061−1064.

[31] PETER L, TOMASZ W, ERWIN P K. Thermo-kinetic prediction of metastable and stable phase precipitation in Al−Zn−Mg series aluminium alloys during non-isothermal DSC analysis [J]. Journal of Alloys and Compounds, 2014, 609(1): 129−136.

[32] LIU G, ZHANG G J, DING X D, SUN J, CHEN K H. Modeling the strengthening response to aging process of

heat-treatable aluminum alloys containing plate/disc- or rod/needle-shaped precipitates [J]. Materials Science and Engineering: A, 2003, 344: 113−124.

[33] CHEN J F, ZHEN L, JIANG J T, YANG L, SHAO W Z, ZHANG B Y. Microstructures and mechanical properties of age-formed 7050 aluminum alloy [J]. Materials Science and Engineering: A, 2012, 539: 115−123.

[34] CAI Yi-xian, ZHAN Li-hua, XU Yong-qian, LIU Chun-hui, WANG Jian-guang, ZHAO Xing, XU Ling-zhi, TONG Can-yu, JIN Geng-quan, WANG Qing, HU La, HUANG Ming-hui. Stress relaxation aging behavior and constitutive modelling of AA7150-T7751 under different temperatures, initial stress levels and pre-strains [J]. Metals, 2019, 9(11): 1215.

[35] YANG You-liang, ZHAN Li-hua, SHEN Ru-lin, LIU Jian, LI Xi-cai, HUANG Ming-hui, HE Di-qiu, CHANG Zhi-long, MA Yun-long, WAN Li. Investigation on the creep-age forming of an integrally-stiffened AA2219 alloy plate experiment and modeling [J]. The International Journal of Advanced Manufacturing Technology, 2018, 95: 2015−2025.

7B50 铝合金双级蠕变时效工艺的新型本构模型及其在回弹预测中的应用

徐凌志[1,2]，童璨瑜[1,3]，刘长志[4]，湛利华[2,3]，黄明辉[2,3]，杨有良[3]，鄢东洋[4]，尹建华[4]，夏 慧[4]，徐永谦[3]

1. 中航通飞华南飞机工业有限公司，珠海 519000；
2. 中南大学 极端服役性能精确制造全国重点实验室，长沙 410083；
3. 中南大学 轻合金研究院，长沙 410083；
4. 北京宇航系统工程研究所，北京 100076

摘 要：针对 Al−Zn−Mg−Cu 合金双级蠕变时效行为建立一套新的统一本构模型。通过考虑不同温度下主要微观特征量演变规律及其相互作用，分析了合金特有的双峰型析出相特征，还引入了位错密度来描述蠕变变形对析出的影响。该模型采用透射电子显微图片的定量分析结果以及先前研究中获得的实验数据进行拟合。随后，本构模型被编译成用户子程序，嵌入有限元软件 ABAQUS 中，用于整体壁板双级蠕变时效工艺过程的模拟和回弹预测。同时进行了相应的整体壁板双级蠕变时效成形实验。测量结果表明，实验成形回弹半径与仿真模拟回弹半径之间的最大偏差小于 0.4 mm，证明所建立的本构模型和有限元模型的有效性。

关键词：双级蠕变时效工艺；双峰型析出相；本构模型；回弹预测；Al−Zn−Mg−Cu 合金

(Edited by Xiang-qun LI)